Operator and entanglement growth in nonthermalizing systems: Many-body localization and the random singlet phase

Ian MacCormack,[1,2,*] Mao Tian Tan,[1,2,†] Jonah Kudler-Flam,[1,2,‡] and Shinsei Ryu[3,§]
[1]*Kadanoff Center for Theoretical Physics, University of Chicago, Chicago, Illinois 60637, USA*
[2]*James Franck Institute, University of Chicago, Chicago, Illinois 60637, USA*
[3]*Department of Physics, Princeton University, Princeton, New Jersey 08540, USA*

(Received 29 March 2020; revised 18 July 2021; accepted 3 September 2021; published 2 December 2021)

We characterize the growth and spreading of operators and entanglement in two paradigmatic nonthermalizing phases—the many-body localized (MBL) phase and the random singlet phase (RSP)—using the entanglement contour and multipartite operator entanglement measures. The entanglement contour characterizes the spacetime spreading of entanglement and reveals logarithmically growing *entanglement light cones* in the MBL and RSP phases, sharply contrasting the linear light cones of clean, thermalizing systems. The operator entanglement characterizes *scrambling*, i.e., the delocalization of information. We find slow scrambling behavior in the MBL phase; the late-time value of the tripartite mutual information scales linearly with system size, but is submaximal. The tripartite logarithmic negativity is also negative and nonzero, but smaller in magnitude, revealing an intriguing distinction between classical and quantum information scrambling in the MBL phase. This is in contrast with the RSP, which, as a noninteracting model, is nonscrambling.

DOI: 10.1103/PhysRevB.104.214202

I. INTRODUCTION

Generically, interacting quantum systems pushed out of equilibrium with some finite energy density rapidly reach equilibrium and become describable (locally) by a thermal ensemble. This can be understood as a process of information delocalization in which the local details of the initial state are spread out, or scrambled, across all degrees of freedom, becoming inaccessible to local measurements.

While most works on quantum chaos and thermalization have focused on systems that obey the eigenstate thermalization hypothesis (ETH) [1,2] and rapidly scramble information, recent studies of disordered systems have found signatures of *slow scrambling* in out-of-time-ordered correlators (OTOCs) [3–11], revealing rich dynamical structure in systems that do not reach thermal equilibrium, or do so exponentially slowly. To better understand slowly scrambling behavior, we analyze the many-body localized (MBL) phase and the random singlet phase (RSP) in two distinct steps: (i) We compute the entanglement contour, which serves as a well-behaved entanglement density function [12], following a global quench to characterize entanglement spreading in spacetime. This reveals emergent *entanglement light cones* distinct from the light cones found in OTOCs. (ii) We compute the tripartite mutual information of the time-evolution operator. This characterizes the extent to which initially localized information delocalizes (scrambles) across the entire system. Two systems with the same entanglement light cone structure may have different behaviors of the operator entanglement. The operator entanglement being nontrivial implies that entanglement is being produced, complexified, and delocalized rather than simply spread around the system coherently. We now review the definitions of these two main actors.

Entanglement contour—The entanglement contour has been shown to provide an intuitive picture of the extent to which each degree of freedom in a given subsystem is entangled with the subsystem's complement. A natural proposal[1] for generic many-body systems is to partition the subsystem, A, into subsets $\{A_i\}$ [14–17]

$$s_A(A_i) \equiv \tfrac{1}{2}[S(A_i|A_1 \cup \cdots \cup A_{i-1}) + S(A_i|A_{i+1} \cup \cdots \cup A_n)], \tag{1}$$

where $S(A|B)$ is the conditional entropy

$$S(A|B) \equiv S(A \cup B) - S(B), \tag{2}$$

and $S(A)$ is the von-Neumann entanglement entropy associated with (the reduced density matrix of) the subsystem A. When we take the continuum limit or consider the contour on a single lattice site, we often use the notation $s_A(x)$, where x denotes the spatial position of A_i. The entanglement contour can be viewed as a well-behaved entanglement density function: $\sum_i s_A(A_i) = S(A)$ or $\int_A dx\, s_A(x) = S(A)$. In other words, the entanglement contour can be viewed as a spatially

*imaccormack@uchicago.edu
†mtan1@uchicago.edu
‡jkudlerflam@uchicago.edu
§shinseir@princeton.edu

[1]Though not uniquely defined, this definition has been shown to give results nearly identical to those of other proposals specific to free systems [13]. Moreover, it has been argued to be unique once an additional physical requirement is imposed [14].

TABLE I. Summary of the results of the paper and other known results about the entanglement contour $s_A(x,t)$ and tripartite operator entanglement (TOMI and TOLN) in various classes of systems. The behavior of the entanglement entropy $S_A(t)$ for a subregion (an interval) A after global quench is also presented. Here, c is the central charge, ϵ is the UV cutoff, and β is the effective temperature of the quench determined by the energy injected to the system. We use the free-fermion CFT as an example of a system with nontrivial entanglement spreading but no scrambling, holographic CFTs as examples of maximal scramblers, and Anderson localized systems as nonscramblers with no entanglement spreading.

System	Half-space $S_A(t)$ after global quench	Half-space $s_A(x,t)$ after global quench	TOMI/TOLN ($t\to\infty$)
Free-fermion CFT	$\frac{1}{12}\ln[\frac{\beta}{\pi\epsilon}\sinh(\frac{2\pi t}{\beta})]$ taking the thermodynamic limit, otherwise there will be revivals [18,19]	$\begin{cases}0, & \lvert x\rvert<2t,\\ \frac{c\pi}{12\beta}\coth(\frac{\pi x}{\beta}), & \lvert x\rvert>2t\end{cases}$ [12,16,20]. This describes a linear light cone.	$I_3=\mathcal{E}_3=0$ [21,22], i.e., no scrambling.
Holographic CFT	$\frac{c}{12}\ln[\frac{\beta}{\pi\epsilon}\sinh(\frac{2\pi t}{\beta})]$ taking the thermodynamic limit, otherwise there will be revivals [23,24]	$\begin{cases}0, & \lvert x\rvert<2t,\\ \frac{c\pi}{12\beta}\coth(\frac{\pi x}{\beta}), & \lvert x\rvert>2t\end{cases}$ [16]. This describes a linear light cone.	$I_3=-2S_A$ [21], $\mathcal{E}_3=-2S_A^{(1/2)}$ [22]. These are thermal entropies and are of the largest magnitude possible, i.e., maximal scrambling.
RSP	Quasi-power-law growth at early times (Fig. 5) and $\ln(\ln(t))$ at very late times [25]	A logarithmic light cone emerges with contour velocity v_c (Fig. 4).	I_3 and $\mathcal{E}_3$ saturate to a constant value, with no length dependence implying no scrambling for large system sizes.
MBL	Logarithmic growth and saturation to subthermal volume-law in finite systems [26–28].	A logarithmic light cone emerges with contour velocity v_c (Fig. 1).	I_3 and $\mathcal{E}_3$ both saturate to macroscopic negative values that scale with the size of region A at exponentially long times with the saturation value of I_3 scaling linearly with A and $\mathcal{E}_3$ potentially sublinearly. Neither are maximal (Fig. 2).
Anderson localization	Rapid saturation to area-law entanglement [26,27].	Information is localized, i.e., no spreading.	$I_3,\mathcal{E}_3\sim 0$, i.e., no scrambling.

resolved version of the entanglement entropy $S(A)$, and, when applied to time-dependent states, it provides a quasilocal picture of how entanglement entropy spreads in a system.

Operator entanglement—To define the operator entanglement [29], we first map the time evolution operator, $U(t)$, to a state in a doubled Hilbert space, $\mathcal{H}_1\otimes\bar{\mathcal{H}}_2$, under the channel-state duality [30,31]. Explicitly, the time evolution operator may be expanded in its energy eigenbasis as

$$U(t)=e^{-iHt}\sum_i |i\rangle\langle i|\,. \tag{3}$$

We can then dualize the bra vector to define the state

$$|U(t)\rangle\rangle=\mathcal{N}e^{-iH_1 t}\sum_i |i\rangle_1|i^*\rangle_2\,, \tag{4}$$

where we take the CPT conjugate, and $\mathcal{N}$ is a normalization factor. The Hamiltonian acts only on the first copy of the Hilbert space. We then compute entanglement measures within this state. Throughout this paper, we let A be a subsystem in the "input" Hilbert space, $\mathcal{H}_1$, and B,C be subsystems in the "output" Hilbert space, $\mathcal{H}_2$, with $B\cup C=\mathcal{H}_2$. Using this partitioning, we can compute the bipartite operator mutual information (BOMI) using the standard definition of mutual information in terms of operator entanglement entropies,

$$I(A,B)=S(A)+S(B)-S(A\cup B), \tag{5}$$

and tripartite operator mutual information (TOMI) by a taking linear combination of BOMIs,

$$I_3(A,B,C)=I(A,B)+I(A,C)-I(A,B\cup C). \tag{6}$$

The TOMI is symmetric about the three regions and diagnoses the extent to which information is delocalized in the quantum channel [32]. Specifically, the negative values of I_3 indicate quantum information spreading.

One disadvantage of the mutual information is that it is sensitive to both quantum and classical correlations. To isolate the quantum information that is scrambled, we compute bipartite operator logarithmic negativity (BOLN), i.e., the logarithmic negativity, $\mathcal{E}(A,B)\equiv\ln(|\rho_{AB}^{T_B}|_1)$, in the operator state. In analogy to TOMI, we also study the tripartite operator logarithmic negativity (TOLN),

$$\mathcal{E}(A:B,C)=\mathcal{E}(A,B)+\mathcal{E}(A,C)-\mathcal{E}(A,B\cup C). \tag{7}$$

The TOLN characterizes the amount of purely quantum information scrambled by the quantum channel. In the MBL phase, we find this to have qualitatively different behavior than the TOMI.

Summary of results

Before proceeding to the details of our analysis, we present Table I, which summarizes our results and contrasts them with previously known results for representative classes of

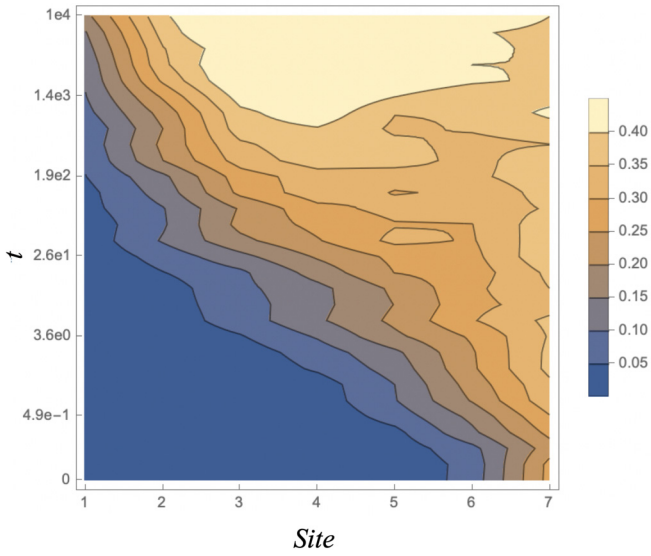

FIG. 1. The entanglement contour after a global quench into H_{LIOM} averaged over 40 disorder realizations, normalized by $\ln 2$, and smoothed out to remove pixelation. The quench was performed from random product states on 14 sites using a disorder strength of $J_0 = 100$. The contour depicted describes the seven leftmost sites. The level sets make the logarithmic entanglement light cone clear (modulo the edge effects occurring at sites 1 and 2).

quantum systems. The upshot is that we find logarithmic light cones for the MBL (Fig. 1) and RSP (Fig. 4) phases. These sharply contrast the linear entanglement light cones observed in, e.g., free theories and CFTs.

Moreover, we find that the exponentially late-time values for the TOMI in the MBL phase are negative and scale linearly with the size of region A but do not saturate the fundamental bounds that are saturated in, e.g., random unitary circuits and holographic conformal field theories [21,22]. The late-time values of TOLN are also negative and nonzero, though they are smaller in magnitude than the associated TOMI values (Fig. 3). This suggests that MBL systems scramble both classical and quantum information nontrivially, albeit exponentially slowly. In contrast, we find the RSP to have trivial TOMI/TOLN, meaning that the RSP channel does not scramble information even though it does spread in spacetime. We attribute this to the free-fermion realization of the RSP that we use.

II. MANY-BODY LOCALIZATION

Many-body localization is perhaps the best known example of ergodicity-breaking in many-body quantum systems. It occurs in interacting systems when an on-site potential is tuned to be sufficiently spatially disordered. MBL has been a subject of intense study in recent years. See, for example, the recent review Ref. [33] and references therein. As the strength of the on-site disorder is increased relative to the interaction strength, more and more of the system's high-energy eigenstates turn from typical volume-law entanglement states (as the eigenstate thermalization hypothesis would imply) to short-range entangled area-law states [34]. Once the localization transition is passed, all eigenstates of the system become

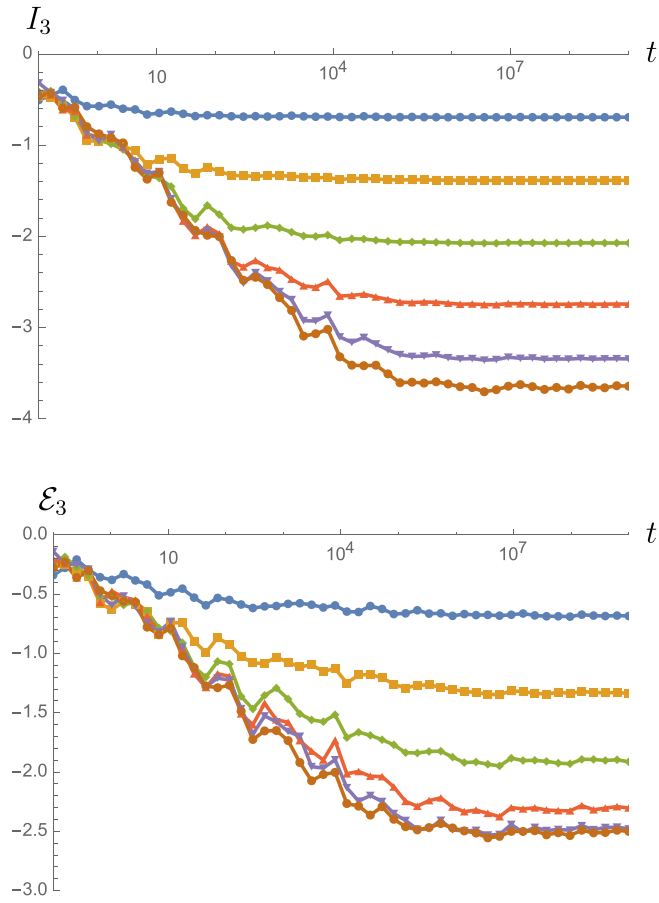

FIG. 2. TOMI (top) and TOLN (bottom) for the H_{LIOM} for a system of 12 input and 12 output qubits for various subinterval sizes. The disorder strength and length scale were chosen so that the LIOM numerics matched the MBL Heisenberg numerics (Fig. 8) for the six-qubit chain. Note the logarithmic timescale and the slow saturation of both quantities, and the larger (negative) magnitude of TOMI compared to TOLN, indicating a reduced spread of quantum vs classical information.

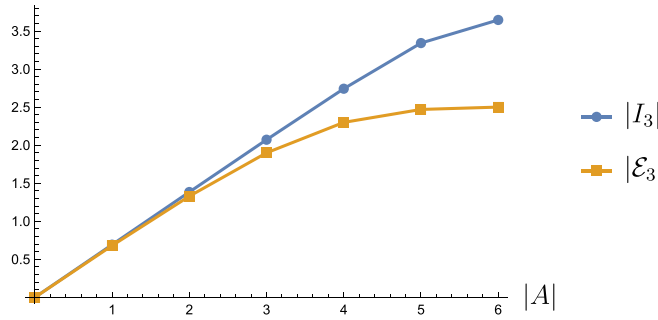

FIG. 3. Late-time saturation values of TOMI and TOLN for the 12-qubit MBL chain, calculated using LIOMs. The saturation values of TOMI fit well to the volume law $I_3(L_A) = \ln(2)L_A$, while the TOLN values grow more slowly in magnitude with system size, indicating suppressed delocalization of quantum information.

area-law entangled, and the system is fully many-body localized. Before reaching the transition, it is possible to have a mobility edge, separating area-law states from volume-law states. In addition to the area-law eigenstates, MBL systems display a number of interesting features. In the localized phase, the systems contain an extensive number of emergent local integrals of motion (LIOMs, sometimes called "l-bits"), with exponentially decaying spatial support. One can write an effective Hamiltonian for the MBL system in terms of these LIOMs [34,35].

MBL systems are also fascinating from a dynamical perspective. Generic interacting many-body quantum systems are thought to be ergodic in the sense that after sufficiently long time evolution, expectation values of local operators become exponentially close to their corresponding thermal expectation values. Thus, memory of the initial state becomes inaccessible to local measurements, and any subsystem can be described by a small number of thermodynamic quantities. MBL systems, on the other hand, do not thermalize. The conserved LIOMs serve to retain memory of the initial state, precluding a description of the late-time state by a thermal ensemble. MBL provides an important counterexample to the eigenstate thermalization hypothesis (ETH) and motivates us to further understand when and how closed quantum systems fail to thermalize. We additionally note that MBL phases and their nonergodic properties have been directly observed in a number of experimental settings [36–38].

Despite their lack of energy and particle transport, MBL systems nevertheless produce nontrivial long-range entanglement in far-from-equilibrium scenarios. For example, if we quench into an MBL Hamiltonian starting from a product state, the entanglement entropy grows logarithmically in time for a time that scales exponentially with the system size [26,27]. After this time, the saturated entanglement entropy in finite systems displays a volume-law, though with a smaller multiplicative coefficient to that of the volume-law for the thermal state [27]. In some sense, this volume-law indicates a partial thermalization of finite-size MBL systems [34]. We are motivated to study this novel entanglement growth more deeply. In particular, we would like to understand how the entanglement spreads at a local level and if/how the information becomes delocalized.

To ensure we capture universal features of the MBL phase, and not artifacts of a particular model, we use the phenomenological MBL fixed point Hamiltonian constructed from the local integrals of motion,

$$H_{\mathrm{LIOM}} = -\sum_i h_i \sigma_i^z - \sum_{i<j} J_{ij}^{(2)} \sigma_i^z \sigma_j^z - \sum_{i<j<k} J_{ijk}^{(3)} \sigma_i^z \sigma_j^z \sigma_k^z + \cdots . \tag{8}$$

Here, the Pauli operators σ_i^z denote emergent local integrals of motion, which are exponentially localized in the physical lattice. For our purposes, we treat them as perfectly localized for the sake of computation. The interaction terms are defined as

$$J_{ij}^{(2)} = \frac{J_{ij}}{2} \exp(-|i-j|/\xi), \quad J_{ijk}^{(3)} = \frac{J_{ijk}}{6} \exp(-|i-k|/\xi), \tag{9}$$

where J_{ij} and J_{ijk} are drawn randomly (from a uniform distribution $[-J_0, J_0]$, with $J_0 = 100$ in our case, but other distributions can be used) and ξ is a dimensionless localization length (which we pick to be 0.5). We also draw h_i from the same distribution. This model was used to compute the OTOC in [5,6].

A. Logarithmic entanglement light cone

We study the entanglement contour after a global quench in order to identify how much entanglement entropy each site contributes to the overall logarithmic growth. Before turning to numerics, we motivate an analytical prediction for the form of the entanglement contour using the language of the emergent LIOMs.

The effective interaction between two "l-bits" separated by a distance d is given by [39]

$$J^{\mathrm{eff}} \sim \mathcal{J} \exp(-d/\xi), \tag{10}$$

where $\mathcal{J}$ is a characteristic interaction strength. Using the effective interaction of the dressed spins, one can obtain an estimate for the amount of time it takes for two unentangled l-bits a distance d apart to become entangled. This happens when $J^{\mathrm{eff}} t \geqslant 1$, so

$$t \sim \frac{1}{\mathcal{J}} \exp(-d/\xi). \tag{11}$$

We now consider an MBL system on a chain of total length L, with a subinterval $[0, \ell]$. Picking a point $x < \ell$ within this subinterval, we can count the number of l-bits outside of the interval with which the l-bit at point x is entangled at a particular time t. This is precisely what the entanglement contour should describe. The result (up to proportionality constants) is

$$s_A(x,t) \propto \begin{cases} 0, & t < \frac{e^{\frac{\ell-x}{\xi}}}{J_0}, \\ \frac{1}{L}\left(\xi \ln(\mathcal{J}t) + x - \ell\right), & \frac{e^{\frac{\ell-x}{\xi}}}{\mathcal{J}} \leqslant t \leqslant \frac{e^{\frac{L-x}{\xi}}}{\mathcal{J}}, \\ 1 - \frac{\ell}{L}, & t > \frac{e^{\frac{L-x}{\xi}}}{\mathcal{J}}. \end{cases} \tag{12}$$

The form of a logarithmic light cone is clear; the wave front of the contour arrives at a time exponential in the distance from the entangling surface $t = \frac{1}{\mathcal{J}} \exp(\frac{\ell-x}{\xi})$. Once this time has passed, the magnitude of the contour increases linearly, saturating at a constant value. This agrees with the observation that entanglement entropy grows logarithmically with time in MBL, eventually reaching a volume-law in the long-time limit. Let us now turn to numerics in order to verify (12).

We select a subinterval consisting of the leftmost seven sites of our 14-site chain, and we compute the entanglement contour of this interval after the global quench using H_{LIOM}. We observe a distinct logarithmic light cone in the entanglement contour in Fig. 1. A similar logarithmic light cone has previously been observed in out-of-time-order correlators (OTOCs) of certain local operators in the MBL phase [7]. These are related but distinct light cones.

The authors of Ref. [7] computed the OTOC as a function of space and time in the disordered Heisenberg model.

Defining the butterfly velocity, v_B, as

$$j_\epsilon \sim v_B \log_{10} t, \tag{13}$$

where j_ϵ is the site at which the wave front of the OTOC has increased past the threshold value of $\epsilon \in (0, 1)$ at time t, they find that v_B depends on both temperature and ϵ, with a slower speed of propagation for lower temperatures. In Refs. [4,5], the authors show that in the MBL LIOM model, the position of the wavefront (up to additive constants and for some suitably defined cutoff) of the OTOC after disorder averaging is given by

$$j_{\text{LIOM}} \propto \xi \log_{10}(t). \tag{14}$$

Our numerical checks for the zero-temperature OTOC indicate that the butterfly velocity for the LIOM model with $\xi = 0.5$, for the initial all $|+\rangle$ product state and for a suitably defined cutoff of 0.5, is $v_B = \frac{\xi}{\log_{10} e} \sim 1.15$.

We can analogously define the contour velocity

$$j_c \sim v_c^\epsilon \log_{10} t, \tag{15}$$

where j_c is the site that the contour wavefront of value $\epsilon \times \tilde{s}^\beta$ has reached. $\tilde{s}^\beta$ is the equilibrium entropy density at effective temperature β which is fixed by the energy of the quench. Using the cutoff $\epsilon = 0.075$, and fitting a line to the wavefront in Fig. 1, we arrive at a contour velocity of $v_c^\epsilon \sim 1.5$ (for analogous results for the disordered Heisenberg model; see Fig. 7 in Appendix A). Like the butterfly velocity, this result is somewhat dependent on the choice of cutoff ϵ, and it may also depend on the choice of initial state. It therefore seems that the contour velocity is larger than the butterfly velocity, but perhaps only marginally so, unlike the case of CFT, where we have the very distinct result $v_c = 2v_B$. A more comprehensive numerical study of the entanglement contour after a global quench in MBL is warranted and could yield a more precise understanding of the relationship between v_B and v_c in MBL. We leave this for future work.

B. Multipartite operator entanglement

Now that we have found that the entanglement spreads according to an emergent logarithmic light cone, we would like to understand what sort of entanglement this really is. Thermalization would necessitate this entanglement to be multipartite, i.e., the information is delocalized throughout the light cone.

We find slow scrambling in the tripartite operator mutual information and tripartite operator logarithmic negativity as seen in Fig. 2. Like many other observables in MBL, TOMI and TOLN take an exponentially long time for the quantities to saturate. While a significant portion of the information in the input channel is delocalized under time evolution, the Haar random values of TOMI and TOLN are never reached.[2] Intriguingly, it appears that the scrambled *quantum information* (TOLN) may scale differently with system size than the *total information* (TOMI). In Fig. 3, we show the saturated values of TOMI and TOLN as a function of input interval size for our 12-site chain. While TOMI scales at or near a volume law (up until half the system size), the magnitude of TOLN is smaller, suggesting the possibility of subvolume law scaling, and indicating that the spreading of quantum correlations is suppressed compared to total correlations. By "total" we are referring to both the quantum and classical (thermal) correlations to which mutual information is sensitive[3] (see, e.g., Ref. [43]). Appendix A contains smaller scale operator entanglement results for the disordered Heisenberg model. To the best of our knowledge, this is a new phenomenon that might be useful in characterizing the quasithermal, late-time state. It would be very interesting to further distinguish this late-time state from conventionally scrambled states. Given the small scales of our numerics, these signatures of novel scrambling behavior may be experimentally accessible in noisy intermediate-scale quantum (NISQ) devices [44] where protocols for preparation of the thermofield double state (4) are being developed [45].

III. RANDOM SINGLET PHASE

In this section, we study the dynamics of a disordered free-fermion model that admits a random singlet phase [46] as its ground state for sufficiently strongly disordered hopping. The RSP infinite-disorder critical point has a number of interesting features, including CFT-like logarithmic scaling of entanglement entropy [47–50], with an effective central charge equal to $\ln 2$ times the central charge of the clean theory. The RSP is the fixed point of the strong disorder real-space renormalization group (SDRG) [51], and it can be seen in, e.g., the antiferromagnetic random bond Heisenberg model [46]. It should be noted, however, that the universal features of the RSP ground state seen at the SDRG fixed point do not necessarily extend to excited states in interacting models [52]. Indeed, while the RSP-like critical behavior extends to the excited states of a noninteracting model like the one we use here (resulting in a so-called "quantum critical glass" [53,54]), small interactions can drive these excited states to an MBL spin-glass phase. Studying the dynamics of an interacting model with a RSP ground state using the entanglement measures in this paper presents an interesting future problem. Some work in this direction has recently been done [55], and it is found that the resulting particle-hole symmetric MBL phase exhibits entanglement growth behavior whose functional form depends on interaction strength, unlike conventional MBL.

Additional work has been done to investigate the dynamics of the random singlet phase. For example, Ref. [25] studied the late-time growth of entanglement entropy in the RSP after a global quench using numerical methods and found it to be doubly logarithmic in time. Other works have studied entanglement growth in disordered critical phases, e.g., Refs. [56,57]. We build upon this work by characterizing the spread and delocalization of information in the RSP.

[2] See Ref. [40] for a discussion on more quantum systems that scramble nonmaximally. We also note that bipartite operator entanglement measures have previously been been studied in MBL systems [26,41].

[3] See Ref. [42] for an interesting comparison between mutual information and negativity in MBL eigenstates.

We use a single-band, free-fermion model with disordered hopping to yield the random singlet phase. The Hamiltonian is

$$H = \sum_i J_i (c_i^\dagger c_{i+1} + c_{i+1}^\dagger c_i), \tag{16}$$

where $J_i \in [0, 1]$ at each bond is drawn independently from the known fixed-point distribution $P(J) = \frac{1}{\delta} J^{-1+1/\delta}$. The parameter δ corresponds to disorder strength. $\delta \to 0$ corresponds to the clean limit, and we approach the infinite randomness fixed point as $\delta \to \infty$. For the purpose of numerics, $\delta = 2.5$ corresponds to sufficiently strong disorder to yield the desired properties of the random singlet phase, and this is the value we use in our simulations.

A. RSP entanglement light cone

We now use the contour to investigate finer-grained aspects of the entanglement entropy growth at long timescales after a quench into the random singlet phase. For our initial state, we use the ground state of the Hamiltonian,

$$H_0 = \sum_i J (c_i^\dagger c_{i+1} + c_{i+1}^\dagger c_i) + \sum_j m_0 (-1)^j c_j^\dagger c_j, \tag{17}$$

which has a gap controlled by the magnitude of m_0. Also note that J is not random in H_0. We use $m_0 = 0.5$ for the initial state of our quench. At $t = 0$, after preparing the ground state at half-filling of (17), we begin to time-evolve with (16). We then compute the entanglement contour at each site, for each time step thereafter. This constitutes our quantum quench.

The entanglement contour generated by the quantum quench described above on a 200-site chain can be seen in Fig. 4. Though the production of entanglement is weaker than it is in the clean limit, the contour demonstrates nontrivial spreading. The smallest discernible values of the entanglement contour (0.001) appear to carve out a logarithmic light cone, consistent with the infinite dynamical critical exponent of the random singlet phase [25]. Between the times 1.75×10^1 and 5.45×10^5, the 0.001 contour fits very well with the function

$$x(t) \sim v_c \log_{10}(t) + x_0, \tag{18}$$

where we find $v_c \sim 3.56$ for the contour velocity.

We also include a plot of the early-time entanglement entropy in Fig. 5 for the above quench configuration. This early-time entanglement entropy growth fits very well with the quasiparticle calculation detailed in Appendix D. The late-time entanglement entropy growth, as computed by summing the contour over its subinterval, is doubly logarithmic, as shown in previous works [25]. We omit this result here and include only the novel, early-time behavior.

B. Multipartite operator entanglement

While the RSP has nontrivial entanglement spreading as demonstrated in the previous section, we still need to determine what sort of entanglement is generated. In particular, is this entanglement multipartite, leading to thermalization of subsystems at late times? Our expectation is that bipartite entanglement should dominate, since our model is free. Indeed,

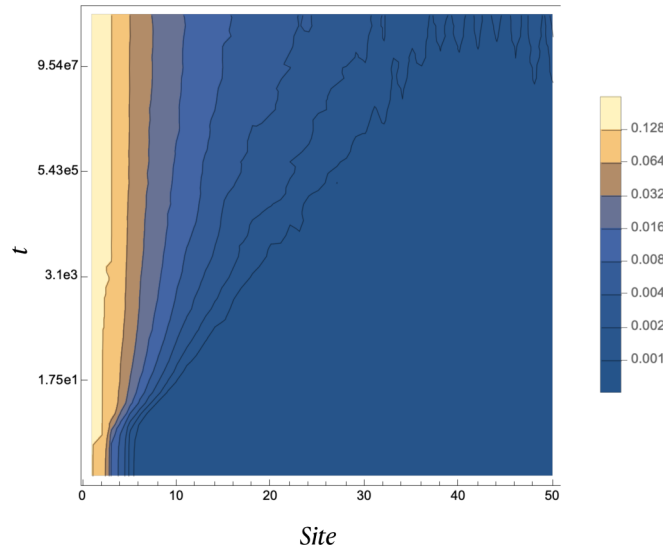

FIG. 4. The entanglement contour for sites 150–200 in an open chain of 200 sites averaged over 5000 disorder realizations and normalized by ln 2 on a semilog plot. We use $m_0 = 0.5$ and a clean hopping for our initial state, and quench into the Hamiltonian (16) with $\delta = 2.5$ and $t = 0$. We see the emergence of a logarithmic light cone for the smaller-valued level sets, consistent with the infinite critical exponent known to occur in the RSP. At very late times ($\sim 10^8$ units of time), we see some deviation from the log light cone in the upper-right hand corner of the plot, likely as a result of finite-size effects.

this is what we find when computing the operator entanglement. We include the details of computing the free-fermion operator entanglement computation in Appendix C. The resulting tripartite operator mutual information and negativity for a 140-site and a 200-site chain are depicted in Fig. 6.

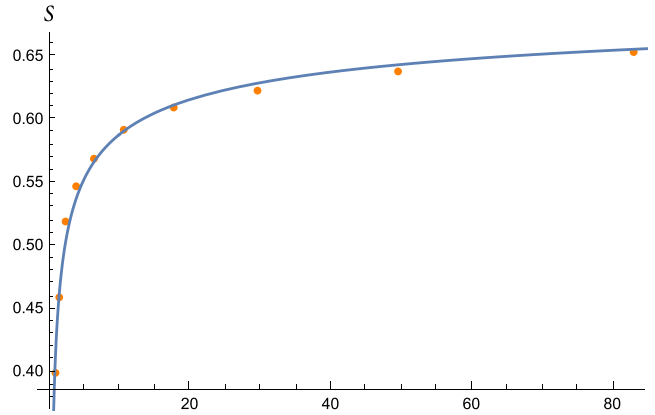

FIG. 5. The quarter chain entanglement entropy for early times after a global quench into the random singlet phase for a system of 200 sites. After an initial linear increase, the entropy grows approximately as a power law before transitioning to a sublogarithmic regime at very long times (not depicted). The numerical results (dots) are averaged over 5000 disorder realizations. The analytic estimate for the entanglement entropy is displayed as a blue line. We fit using $\beta_{\text{eff}} = 0.1972$. The analytic estimates derived from the quasiparticle picture show excellent agreement with the numerics.

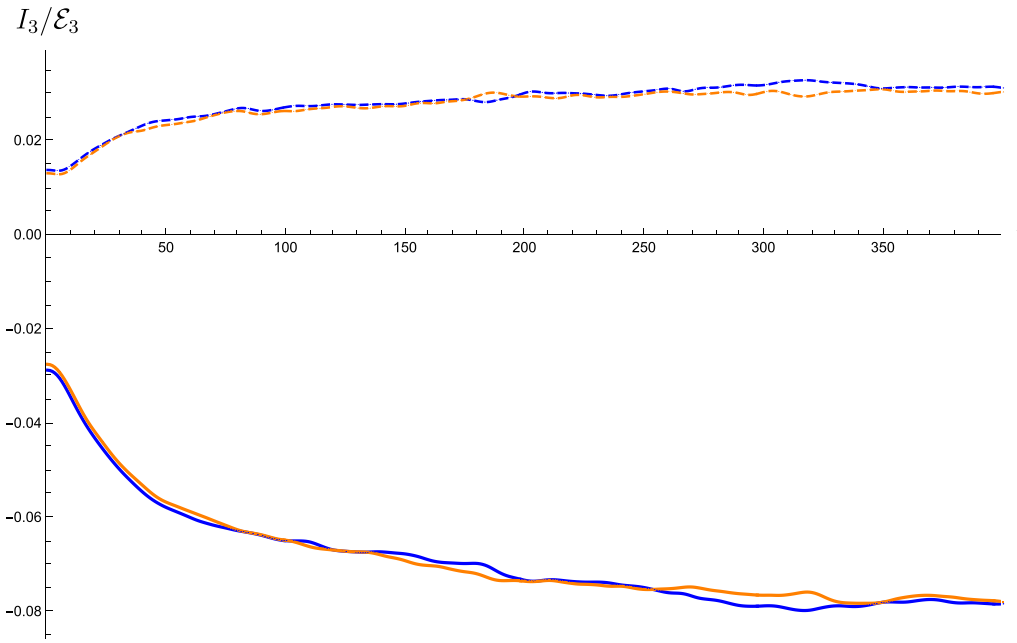

FIG. 6. The tripartite operator mutual information (solid lines) and negativity (dashed lines) for a 140-site (blue) and a 200-site (orange) chain, for a half-chain input subsystem. The results were averaged over 1500 disorder realizations with disorder strength $\delta = 2.5$. Both quantities are very small in magnitude and independent of system size, indicating a lack of scrambling, as expected in a free-fermion system.

While the tripartite mutual information is slightly negative and appears to saturate at some value that is independent of the subsystem size, this is merely a finite-size effect, and this model of the random singlet phase, despite its interesting bipartite entanglement dynamics, cannot scramble information, as it is a free-fermion model. This is further demonstrated by the very small, positive values of TOLN that are independent of system size.

IV. DISCUSSION

In summary, we have investigated the nonequilibrium dynamics of two distinct nonthermalizing phases: a local integral of motion model of many-body localization, and (a free-fermion realization of) the random singlet phase.

Entanglement light-cone behavior—Calculating the entanglement contour after a global quench revealed a logarithmic light cone of entanglement spreading in MBL. This light cone was similar, but not identical, to the logarithmic light cone seen for the OTOC [58]. Meanwhile, in the RSP, the entanglement contour yielded a logarithmic light cone, despite trivial spreading of the OTOC in that system. Each light cone defines a velocity, and we now comment on how these may be related or distinguished. Following a global quantum quench, the entanglement contour propagates from the entangling surfaces. The contour velocity is the speed at which the wavefront propagates. One must impose some cutoff value of the contour in order to define the wavefront. On the other hand, the butterfly velocity corresponds to the speed at which local operators spread, in contrast to the contour velocity, which corresponds to the speed at which correlations spread. The butterfly velocity is defined through the OTOC. Naturally, the contour velocity and butterfly velocity will be related. They are, in general, different speeds partially because the OTOC only time evolves one of the operators in the correlation function, while the entanglement contour probes time-evolved *states*, i.e., all operators are time-evolved. Because all operators have been given the chance to spread in time, the contour velocity will typically be higher than the butterfly velocity. In 2D conformal field theories, it is true that $v_c = 2v_B$. [16]. The proportionality constant appears to be smaller in the case of the MBL LIOM model, though the factor of 2 does appear to approximately hold (in logarithmic time) for the disordered Heisenberg model (included in Appendix A). We believe it would be interesting to study the relationship between v_c and v_B in more general systems.

Late-time quasiequilibration—To characterize the kind of entanglement generated by time evolution, we calculated operator mutual information and negativity for both phases. We found that the many-body localized system demonstrated slow but nontrivial saturation of tripartite operator mutual information and negativity, to values smaller in magnitude than the Haar-random case. The late-time values of TOLN were even further suppressed. This indicates a level of weakly scrambled quasiequilibration in MBL. However, the late-time state is clearly not fully thermalized because it still retains memory of the initial LIOMs. We wonder whether this is a different sort of "thermalized" quasiequilibrium state and whether it can be characterized by a generalized Gibbs ensemble or a generalization of the so-called canonical thermal pure quantum (cTPQ) states [59].

In contrast to the MBL phase, we found the RSP to demonstrate multipartite operator measures that decayed to zero with increasing disorder, indicating that despite nontrivial entanglement spreading, the RSP does not delocalize quantum information. This is unsurprising, as we used a

free-fermion model for the RSP. Our results indicate a broad range of behavior of state and operator dynamics lying between clean, free-particle systems and the maximally scrambling holographic or Haar-random systems. Other intermediate systems that may be worth investigating include models with quasiperiodic potentials (in particular, the Aubry-André model [60]), Floquet systems, and random unitary circuits with measurements.[4]

As entanglement measures become more experimentally accessible, the ubiquity of disorder in physical systems could make slowly scrambling systems an interesting testbed for quantum information dynamics in the laboratory. Many-body localization has been realized experimentally in several different settings, including superconducting qubits [67] and optical lattice systems [68]. Information theoretic measures, for example the quantum Fisher information [36] and the second Rényi entanglement entropy [38,69], have become measurable in the laboratory. As experiments continue to improve, we hope to see the finer-grained probes of entanglement spreading and scrambling that we have studied measured experimentally in MBL and other disordered systems.

Note added. During the completion of this work, a paper appeared that also studies operator entanglement in MBL systems using an effective Hamiltonian [70]. That Hamiltonian is distinct from the one we study in Sec. II.

ACKNOWLEDGMENTS

We thank Dmitry Abanin, Masahiro Nozaki, Hassan Shapourian, and Masaki Tezuka for useful comments. S.R. is supported by a Simons Investigator Grant from the Simons Foundation. This work was supported by the National Science Foundation under Award No. DMR-2001181, and by a Simons Investigator Grant from the Simons Foundation (Award No. 566116).

APPENDIX A: DISORDERED HEISENBERG MBL RESULTS

Here we present supplementary entanglement contour and operator entanglement results for the many-body localized disordered Heisenberg model, which has the following Hamiltonian:

$$H = J\sum_i \left(\sigma_i^x\sigma_{i+1}^x + \sigma_i^y\sigma_{i+1}^y + \sigma_i^z\sigma_{i+1}^z\right) + \sum_i h_i\sigma_i^z, \quad \text{(A1)}$$

where h_i is a random variable from the uniform distribution $[-h, h]$. This model is believed to be fully many-body localized for $J = 1$ and $h \gtrsim 7$. As in Ref. [7], we will use $h = 16$ to ensure a short localization length.

We first present the entanglement contour, in Fig. 7, which, though demonstrating slightly different features than the LIOM light cone in Fig. 1, retains the essential logarithmic light cone, this time with a contour velocity of $1 \lesssim v_c \lesssim 2$ if measured along the 0.002 or the 0.004 contours. Here, the contour velocity appears to depend on the choice of cutoff,

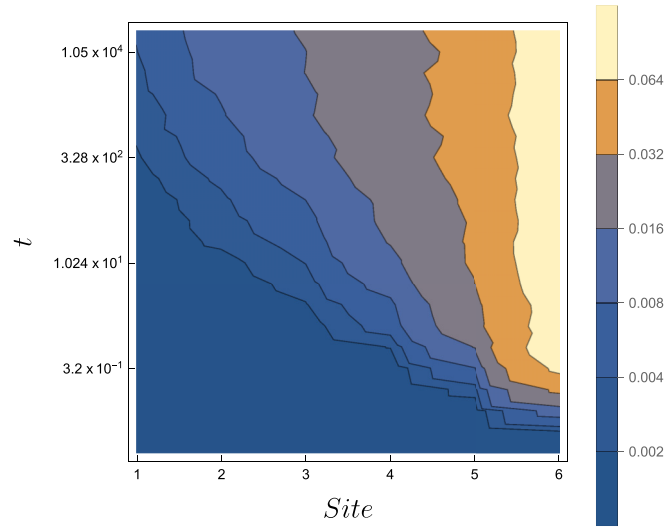

FIG. 7. The entanglement contour for the leftmost six-site subinterval (divided by $\ln 2$) in the MBL Heisenberg model after quenching from random product states. The results were averaged over 400 disorder realizations.

and the overall magnitude of entanglement is lower. This may be a model-dependent effect.

Next, we present the exact diagonalization results of the operator mutual information and negativity in the disordered Heisenberg model. Because we must directly compute and partially trace over the operator-state density matrix, we are limited to a system size of six spins. The results for TOMI and TOLN are depicted in Fig. 8. These results were computed before the LIOM results, and the dramatic difference in the scaling of TOMI and TOLN motivated further calculations using LIOMs.

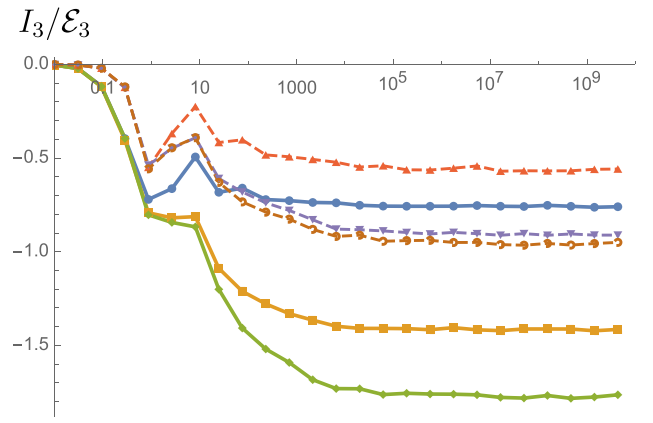

FIG. 8. TOMI (solid lines) and TOLN (dashed lines) computed for a six-site random Heisenberg model for input intervals of one, two, and three sites. As in the case of LIOM calculation, both values saturate exponentially slowly, and the larger (negative) magnitude of the TOMI saturation value suggests a suppression of quantum information spreading.

[4]See, e.g., Refs. [11,61–66] for examples of recent work in this direction.

APPENDIX B: COMPUTING OPERATOR ENTANGLEMENT AND NEGATIVITY WITH MBL INTEGRALS OF MOTION

We will use the LIOM basis to compute operator mutual information for a MBL system. We start with the following Hamiltonian:

$$H_{\mathrm{LIOM}} = -\sum_i h_i \sigma_i^z - \sum_{i<j} J_{ij}^{(2)} \sigma_i^z \sigma_j^z - \sum_{i<j<k} J_{ijk}^{(3)} \sigma_i^z \sigma_j^z \sigma_k^z, \tag{B1}$$

where we have truncated terms beyond third order. In the LIOM basis, the time evolution operator for a chain of N spins is

$$\begin{aligned} U &= \sum_{\{s\}} e^{-itH_{\mathrm{LIOM}}(s)} |s_1 \cdots s_N\rangle\langle s_1 \cdots s_N|, \\ H_{\mathrm{LIOM}}(s) &= -\sum_i h_i s_i - \sum_{i<j} J_{ij}^{(2)} s_i s_j - \sum_{i<j<k} J_{ijk}^{(3)} s_i s_j s_k, \end{aligned} \tag{B2}$$

where $\sum_{\{s\}}$ is a sum over all 2^N classical spin configurations. Since U is already diagonal in the LIOM basis, we can replace the Pauli operators in the Hamiltonian with classical spin values. To compute operator entanglement measures we use the channel-state duality to obtain the U operator state, and then we take the outer product to get the density matrix of the doubled Hilbert space state,

$$\rho_U = \sum_{\{s\},\{s'\}} e^{it[H_{\mathrm{LIOM}}(s) - H_{\mathrm{LIOM}}(s')]} |s_1 \cdots s_N\rangle\langle s'_1 \cdots s'_N|, \tag{B3}$$

where $|s_1 \cdots s_N\rangle$ labels collectively spin configurations in the input and output Hilbert spaces, for brevity. We can go further by subdividing the input and output Hilbert spaces into intervals A, D and B, C, respectively:

$$\begin{aligned} \rho_U = \sum_{\{s\},\{s'\}} & e^{it[H_{\mathrm{LIOM}}(s) - H_{\mathrm{LIOM}}(s')]} \\ & \times |\{s\}_A, \{s\}_B, \{s\}_C, \{s\}_D\rangle\langle\{s'\}_A, \{s'\}_B, \{s'\}_C, \{s'\}_D|. \end{aligned} \tag{B4}$$

We choose A and B to be of the same size and position in their respective Hilbert spaces. To obtain a reduced density matrix for the operator state—for example for $A \cup B$—we can trace out $C \cup D$,

$$\begin{aligned} \rho_{AB} = & \sum_{\{s\}_A,\{s\}_B,\{s'\}_A,\{s'\}_B} \sum_{\{s\}_C,\{s\}_D} \\ & \times e^{it[H_{\mathrm{LIOM}}(s_A,s_B,s_C,s_D) - H_{\mathrm{LIOM}}(s'_A,s'_B,s_C,s_D)]} \\ & \times |\{s\}_A, \{s\}_B\rangle\langle\{s'\}_A, \{s'\}_B|. \end{aligned} \tag{B5}$$

By performing the sums over s_C and s_D to calculate the matrix elements of ρ_{AB}, we can avoid directly storing and tracing over a $2^{2N} \times 2^{2N}$ matrix, and instead deal with, at most, a $2^N \times 2^N$ matrix. This is not a dramatic decrease in numerical overhead, but it allows us to (nearly) double the size of the system in question when computing operator entanglement measures, as compared to directly performing the partial trace over the full operator state density matrix.

APPENDIX C: OPERATOR ENTANGLEMENT AND NEGATIVITY FOR FREE FERMIONS

In this Appendix, we present a review of how to compute operator entanglement measures for free-fermion systems using the correlator method.

1. Operator state for free fermions

We wish to compute the operator mutual information for the following state:

$$|U_\beta(t)\rangle = e^{-\frac{it}{2}(H_1+H_2)} |TFD_\beta\rangle \tag{C1}$$

for a free-fermion Hamiltonian with no superconducting terms

$$\hat{H} = \sum_{i,j=1}^{L} H_{i,j} c_i^\dagger c_j. \tag{C2}$$

We can diagonalize this Hamiltonian with a unitary matrix U, so $H = UDU^\dagger$:

$$\hat{H} = \underbrace{c_i^\dagger U_{ik}}_{\equiv \psi_k^\dagger} D_{kl} \underbrace{U_{lj}^\dagger c_j}_{\equiv \psi_l} = \psi_k^\dagger D_{kl} \psi_l = \epsilon_k \psi_k^\dagger \psi_k. \tag{C3}$$

We then write down the thermofield double state with the fermions in the diagonal basis,

$$\begin{aligned} |TFD_\beta\rangle &= \frac{1}{\sqrt{Z}} \prod_k \left(\sum_{i_k} e^{-\frac{\beta}{2}\epsilon_k \psi_k^\dagger \psi_k} |i_k\rangle\, |i_k^*\rangle \right) \\ &= \frac{1}{\sqrt{Z}} \prod_k (1 + e^{-\frac{\beta}{2}\epsilon_k} \psi_{Ak}^\dagger \psi_{Bk}^\dagger) |0\rangle . \end{aligned} \tag{C4}$$

Requiring $\langle TFD_\beta | TFD_\beta\rangle = 1$ fixes the normalization factor as $Z = \prod_k (1 + e^{-\beta\epsilon_k})$. The normalized thermofield double state is thus

$$|TFD_\beta\rangle = \prod_k \left(\underbrace{\frac{e^{\frac{\beta}{2}\epsilon_k}}{\sqrt{1+e^{\beta\epsilon_k}}}}_{\equiv \cos\theta_k} + \underbrace{\frac{1}{\sqrt{1+e^{\beta\epsilon_k}}}}_{\equiv \sin\theta_k} \psi_{Ak}^\dagger \psi_{Bk}^\dagger \right) |0\rangle \tag{C5}$$

and the time-evolved operator state becomes

$$|U(t)\rangle = \prod_k (\cos\theta_k + \sin\theta_k e^{-it\epsilon_k} \psi_{Ak}^\dagger \psi_{Bk}^\dagger) |0\rangle . \tag{C6}$$

Alternate form of the operator state—We now rewrite the operator state (C6) by using the holes of the B Hilbert space instead of the particles because this allows us to use the regular correlation matrix without pairing terms. Let χ_{Ak}, χ_{Bk} be new fermion operators and consider

$$\begin{aligned} & \prod_k \left(\cos\theta_k \chi_{Bk}^\dagger + \sin\theta_k e^{-it\epsilon_k} \chi_{Ak}^\dagger\right) |0\rangle_\chi \\ & \quad = \prod_k \left(\cos\theta_k + \sin\theta_k e^{-it\epsilon_k} \chi_{Ak}^\dagger \chi_{Bk}\right) \prod_q \chi_{Bq}^\dagger |0\rangle_\chi . \end{aligned} \tag{C7}$$

We now define $\chi_{Ak} = \psi_{Ak}$, $\chi_{Bk} = \psi_{Bk}^\dagger$, and note $|0\rangle_\psi \sim \prod_q \chi_{Bq}^\dagger |0\rangle_\chi$ because $\psi_{Bp} |0\rangle_\psi \sim \chi_{Bp}^\dagger \prod_q \chi_{Bq}^\dagger |0\rangle_\chi = 0$, since $(\chi^\dagger)^2 = 0$. The ψ and χ fermions are related by a particle-hole transformation on H_B. The state (C7) is already

normalized. In terms of the χ_{Ik} fermions, we have

$$|U(t)\rangle = \prod_k (\cos\theta_k \chi^\dagger_{Bk} + \sin\theta_k e^{-it\epsilon_k}\chi^\dagger_{Ak})\,|0\rangle\,, \tag{C8}$$

where it is understood that $|0\rangle = |0\rangle_\chi$.

2. Correlator method

Now we compute the correlation matrix

$$\langle U(t)|\,\chi^\dagger_{Ik}\chi_{Jk'}\,|U(t)\rangle = \delta_{kk'}\,\langle U(t)|\,\chi^\dagger_{Ik}\chi_{Jk}\,|U(t)\rangle\,, \tag{C9}$$

where we noted that if $k \neq k'$, $\chi^\dagger_{Ik}\chi_{Jk'} = -\chi_{Jk'}\chi^\dagger_{Ik}$ annihilates $|U(t)\rangle$. Suppose that the product over the modes in (C8) is arranged in increasing order. The matrix element for each mode k can be computed from

$$\begin{aligned}\langle U(t)|\,\chi^\dagger_{Ik}\chi_{Jk}\,|U(t)\rangle = \langle 0|\prod_{q>k}(\cos\theta_q\chi_{Bq} + \sin\theta_q e^{it\epsilon_q}\chi_{Aq})\\ \times\,[(\cos\theta_k\chi_{Bk} + \sin\theta_k e^{it\epsilon_k}\chi_{Ak})\chi^\dagger_{Ik}\chi_{Jk}\\ \times\,(\cos\theta_k\chi^\dagger_{Bk} + \sin\theta_k e^{-it\epsilon_k}\chi^\dagger_{Ak})]\\ \times\prod_{p>k}(\cos\theta_p\chi^\dagger_{Bp} + \sin\theta_p e^{-it\epsilon_p}\chi^\dagger_{Ap})\,|0\rangle\end{aligned} \tag{C10}$$

for the four possible values of (I, J). The correlation matrix in this basis is thus

$$\begin{aligned}&\langle U(t)|\,\chi^\dagger_{Ik}\chi_{Jk'}\,|U(t)\rangle\\ &\quad= \delta_{kk'}\begin{pmatrix}\sin^2\theta_k & \sin\theta_k\cos\theta_k e^{it\epsilon_k}\\ \sin\theta_k\cos\theta_k e^{-it\epsilon_k} & \cos^2\theta_k\end{pmatrix}.\end{aligned} \tag{C11}$$

The correlation matrix in real space, which we need for the calculation of the entanglement entropy, is given by

$$\begin{aligned}&\langle U(t)|\,\chi^\dagger_{Ix}\chi_{Jx'}\,|U(t)\rangle\\ &\quad= \sum_k V^*_{xk}\begin{pmatrix}\sin^2\theta_k & \sin\theta_k\cos\theta_k e^{it\epsilon_k}\\ \sin\theta_k\cos\theta_k e^{-it\epsilon_k} & \cos^2\theta_k\end{pmatrix}V^t_{kx'},\end{aligned} \tag{C12}$$

where a general position space Hamiltonian can be diagonalized through the unitary matrix as

$$\begin{aligned}\hat{H} &= \sum_{x,y}\chi^\dagger_x H_{xy}\chi_y = \sum_{x,y}\underbrace{\chi^\dagger_x V_{xk}}_{\chi^\dagger_k}\underbrace{D_{kq}}_{\epsilon_k\delta_{kq}}\underbrace{V^\dagger_{qy}\chi_y}_{\chi_q}\\ &= \sum_k \epsilon_k\chi^\dagger_k\chi_k,\end{aligned} \tag{C13}$$

Finally, the Von Neumann entropy is given by

$$S(t) = -\sum_n [\xi_n(t)\ln\xi_n(t) + [1-\xi_n(t)]\ln(1-\xi_n(t))], \tag{C14}$$

where $\xi_k(t)$ are the eigenvalues of the correlation matrix truncated to the entries corresponding to degrees of freedom in our subsystem.

APPENDIX D: QUASIPARTICLES FOR THE RSP

The early-time entanglement entropy growth is depicted in Fig. 5. Qualitatively, we see an initial linear growth, followed by what appears to be a power-law growth, which eventually settles to a very slow, sublogarithmic growth. To obtain an analytical estimate for the entanglement dynamics, we use the quasiparticle picture that is applicable to integrable systems [18,71–73]. The master formula is

$$S(t) \propto t\int_{|v(\varepsilon)|t<\ell} d\varepsilon v(\varepsilon)f(\varepsilon) + \ell\int_{|v(\varepsilon)|t>\ell} d\varepsilon f(\varepsilon), \tag{D1}$$

where ℓ is the length of the interval, $v(\varepsilon)$ is the velocity of the quasiparticles at energy ε, and $f(\varepsilon)$ is the entanglement production rate of quasiparticles. In other words, $f(\varepsilon)$ is the extent to which each mode contributes to the entanglement entropy. For this function, we can use the entropy of each occupied fermionic mode,

$$f(\varepsilon) = -[1-n(\varepsilon)]\ln[1-n(\varepsilon)] - n(\varepsilon)\ln n(\varepsilon), \tag{D2}$$

where $n(\varepsilon)$ is the occupation number of each mode after the quench. We use the Fermi-Dirac distribution

$$n(\varepsilon) = \frac{1}{1+e^{\beta_{eff}\varepsilon}}, \tag{D3}$$

which provides an excellent approximation. Here, β_{eff} is an effective inverse temperature, determined by the energy of the initial state.

Using the density of states for the SDRG fixed point, $\rho(\varepsilon)$ [74], we can compute the velocity of the associated quasiparticles

$$\rho(\varepsilon) = \frac{\rho_0}{\varepsilon|\ln\varepsilon|^3} \to v(\varepsilon) = \frac{\varepsilon|\ln\varepsilon|^3}{\rho_0}. \tag{D4}$$

The above density of states is quite unusual, though we have verified it numerically, reassuring us that we are closely approximating the infinite disorder fixed point. It displays a concentration of low-energy "slow" modes between $\varepsilon = 0$ and 1. These may be responsible for the long-time growth of entanglement entropy. It should be emphasized, however, that the above density of states comes from the fixed point of a real-space RG procedure, and is only expected to be valid asymptotically as $\varepsilon \to 0$. Using the standard form for the semiclassical particle velocity, $v(\varepsilon) = d\varepsilon(k)/dk|_{k(\varepsilon)}$, which we have done, is also not exactly correct, since the eigenstates of the disordered model are not labeled by momentum k. Disorder averaging, however, restores approximate translational symmetry, and the above form of the quasiparticle velocities yields results consistent with numerics. Combining the ingredients from (D1)–(D4), we obtain the integral

$$\begin{aligned}S(t) \propto \frac{t}{\rho_0}\left[\int_{|v(\varepsilon)|t<\ell} d\varepsilon\varepsilon|\ln\varepsilon|^3 + \ell\int_{|v(\varepsilon)|t>\ell} d\varepsilon\right]\\ \times\left[\ln(1+e^{\beta\varepsilon}) - \frac{\beta\varepsilon e^{\beta\varepsilon}}{1+e^{\beta\varepsilon}}\right].\end{aligned} \tag{D5}$$

To second order in β, the first integral is

$$\frac{t}{\rho_0}\int_{|v(\varepsilon)|t<\ell} d\varepsilon\varepsilon|\ln\varepsilon|^3\left(\ln 2 - \frac{\varepsilon^2\beta^2}{8} + O(\beta^4)\right), \tag{D6}$$

which is much easier to deal with. To determine the integration bounds, we solve

$$v(\varepsilon)t = \frac{\varepsilon|\ln\varepsilon|^3 t}{\rho_0} = \ell \tag{D7}$$

for $\varepsilon > 0$. Because $v(\varepsilon)$ does not increase monotonically with ε, there are multiple branches to the solution: $\exp[3W_{-1}(\frac{-1}{3}\sqrt[3]{\frac{\ell}{t}})]$, $\exp[3W(\frac{-1}{3}\sqrt[3]{\frac{\ell}{t}})]$, and $\exp[3W(\frac{1}{3}\sqrt[3]{\frac{\ell}{t}})]$, where $W_k(x)$ is the kth branch of the product log or Lambert W-function, and $W(x)$ is the principal branch of the product log function. The first two solutions are only valid (real) for $t > t^* = \frac{e^3\ell}{27}$, while the third is valid for all $t > 0$. Thus, t^* is the time at which the slow modes begin to contribute to the entanglement growth. This set of slow modes makes the dynamics of the RSP markedly different from that of free fermions.

The second term in (D5) can be integrated exactly. Taking into account, once again, the multiple domains of integration, and imposing an energy cutoff ϵ (which also functions as a velocity cutoff), we obtain a very complicated and unenlightening expression for the entanglement entropy, which we have used to fit the numerical data in Fig. 5.

[1] J. M. Deutsch, Quantum statistical mechanics in a closed system, Phys. Rev. A **43**, 2046 (1991).

[2] M. Srednicki, Chaos and quantum thermalization, Phys. Rev. E **50**, 888 (1994).

[3] R. Fan, P. Zhang, H. Shen, and H. Zhai, Out-of-time-order correlation for many-body localization, Sci. Bull. **62**, 707 (2017).

[4] Y. Chen, Universal logarithmic scrambling in many body localization, arXiv:1608.02765.

[5] X. Chen, T. Zhou, D. A. Huse, and E. Fradkin, Out-of-time-order correlations in many-body localized and thermal phases, Ann. Phys. **529**, 1600332 (2017).

[6] B. Swingle and D. Chowdhury, Slow scrambling in disordered quantum systems, Phys. Rev. B **95**, 060201(R) (2017).

[7] Y. Huang, Y.-L. Zhang, and X. Chen, Out-of-time-ordered correlators in many-body localized systems, Ann. Phys. **529**, 1600318 (2017).

[8] A. Nahum, J. Ruhman, and D. A. Huse, Dynamics of entanglement and transport in one-dimensional systems with quenched randomness, Phys. Rev. B **98**, 035118 (2018).

[9] V. Khemani, A. Vishwanath, and D. A. Huse, Operator Spreading and the Emergence of Dissipative Hydrodynamics Under Unitary Evolution with Conservation Laws, Phys. Rev. X **8**, 031057 (2018).

[10] S. Sahu, S. Xu, and B. Swingle, Scrambling Dynamics Across a Thermalization-Localization Quantum Phase Transition, Phys. Rev. Lett. **123**, 165902 (2019).

[11] S. Xu, X. Li, Y.-T. Hsu, B. Swingle, and S. Das Sarma, Butterfly effect in interacting Aubry-Andre model: Thermalization, slow scrambling, and many-body localization, Phys. Rev. Research **1**, 032039(R) (2019).

[12] Y. Chen and G. Vidal, Entanglement contour, J. Stat. Mech.: Theor. Exp. (2014) 10011.

[13] J. Kudler-Flam, H. Shapourian, and S. Ryu, The negativity contour: A quasi-local measure of entanglement for mixed states, SciPost Phys. **8**, 063 (2020).

[14] Q. Wen, Formulas for partial entanglement entropy, Phys. Rev. Research **2**, 023170 (2020).

[15] Q. Wen, Fine structure in holographic entanglement and entanglement contour, Phys. Rev. D **98**, 106004 (2018).

[16] J. Kudler-Flam, I. MacCormack, and S. Ryu, Holographic entanglement contour, bit threads, and the entanglement tsunami, J. Phys. A **52**, 325401 (2019).

[17] Q. Wen, Entanglement contour from subset entanglement entropies, J. High. Energ. Phys. 05 (2020) 018.

[18] P. Calabrese and J. Cardy, Evolution of entanglement entropy in one-dimensional systems, J. Stat. Mech.: Theor. Exp. (2005) 04010.

[19] J. Cardy, Thermalization and Revivals After a Quantum Quench in Conformal Field Theory, Phys. Rev. Lett. **112**, 220401 (2014).

[20] G. Di Giulio, R. Arias, and E. Tonni, Entanglement Hamiltonians in 1D free lattice models after a global quantum quench, J. Stat. Mech. (2019) 123103.

[21] L. Nie, M. Nozaki, S. Ryu, and M. Tian Tan, Signature of quantum chaos in operator entanglement in 2d CFTs, J. Stat. Mech.: Theor. Exp. (2019) 093107.

[22] J. Kudler-Flam, M. Nozaki, S. Ryu, and M. T. Tan, Quantum vs. classical information: Operator negativity as a probe of scrambling, J. High Energy Phys. 01 (2020) 031.

[23] T. Hartman and J. Maldacena, Time evolution of entanglement entropy from black hole interiors, J. High Energy Phys. 05 (2013) 014.

[24] G. Mandal, R. Sinha, and T. Ugajin, Finite size effect on dynamical entanglement entropy: CFT and holography, arXiv:1604.07830.

[25] F. Iglói, Z. Szatmári, and Y.-C. Lin, Entanglement entropy dynamics of disordered quantum spin chains, Phys. Rev. B **85**, 094417 (2012).

[26] M. Žnidarič, T. Prosen, and P. Prelovšek, Many-body localization in the Heisenberg XXZ magnet in a random field, Phys. Rev. B **77**, 064426 (2008).

[27] J. H. Bardarson, F. Pollmann, and J. E. Moore, Unbounded Growth of Entanglement in Models of Many-Body Localization, Phys. Rev. Lett. **109**, 017202 (2012).

[28] M. Serbyn, Z. Papić, and D. A. Abanin, Universal Slow Growth of Entanglement in Interacting Strongly Disordered Systems, Phys. Rev. Lett. **110**, 260601 (2013).

[29] P. Zanardi, Entanglement of quantum evolutions, Phys. Rev. A **63**, 040304(R) (2001).

[30] M.-D. Choi, Completely positive linear maps on complex matrices, Lin. Alg. Appl. **10**, 285 (1975).

[31] A. Jamiolkowski, Linear transformations which preserve trace and positive semidefiniteness of operators, Rep. Math. Phys. **3**, 275 (1972).

[32] P. Hosur, X.-L. Qi, D. A. Roberts, and B. Yoshida, Chaos in quantum channels, J. High Energy Phys. 02 (2016) 004.

[33] D. A. Abanin and Z. Papić, Recent progress in many-body localization, Ann. Phys. **529**, 1700169 (2017).

[34] M. Serbyn, Z. Papić, and D. A. Abanin, Local Conservation Laws and the Structure of the Many-Body Localized States, Phys. Rev. Lett. **111**, 127201 (2013).

[35] D. A. Huse, R. Nandkishore, and V. Oganesyan, Phenomenology of fully many-body-localized systems, Phys. Rev. B **90**, 174202 (2014).

[36] J. Smith, A. Lee, P. Richerme, B. Neyenhuis, P. W. Hess, P. Hauke, M. Heyl, D. A. Huse, and C. Monroe, Many-body localization in a quantum simulator with programmable random disorder, Nat. Phys. **12**, 907 (2016).

[37] R. Islam, R. Ma, P. M. Preiss, M. E. Tai, A. Lukin, M. Rispoli, and M. Greiner, Measuring entanglement entropy in a quantum many-body system, Nature **528**, 77 (2015).

[38] A. Lukin, M. Rispoli, R. Schittko, M. E. Tai, A. M. Kaufman, S. Choi, V. Khemani, J. Léonard, and M. Greiner, Probing entanglement in a many-body-localized system, Science **364**, 256 (2019).

[39] R. Nandkishore and D. A. Huse, Many-body localization and thermalization in quantum statistical mechanics, Annu. Rev. Condens. Matter Phys. **6**, 15 (2015).

[40] J. Kudler-Flam, L. Nie, and S. Ryu, Conformal field theory and the web of quantum chaos diagnostics, J. High Energy Phys. 01 (2020) 175.

[41] T. Zhou and D. J. Luitz, Operator entanglement entropy of the time evolution operator in chaotic systems, Phys. Rev. B **95**, 094206 (2017).

[42] J. Gray, A. Bayat, A. Pal, and S. Bose, Scale invariant entanglement negativity at the many-body localization transition, arXiv:1908.02761.

[43] J. Gray, S. Bose, and A. Bayat, Many-body localization transition: Schmidt gap, entanglement length, and scaling, Phys. Rev. B **97**, 201105(R) (2018).

[44] J. Preskill, Quantum computing in the NISQ era and beyond, Quantum **2**, 79 (2018).

[45] J. Wu and T. H. Hsieh, Variational Thermal Quantum Simulation Via Thermofield Double States, Phys. Rev. Lett. **123**, 220502 (2019).

[46] D. S. Fisher, Random antiferromagnetic quantum spin chains, Phys. Rev. B **50**, 3799 (1994).

[47] G. Refael and J. E. Moore, Entanglement Entropy of Random Quantum Critical Points in One Dimension, Phys. Rev. Lett. **93**, 260602 (2004).

[48] N. Laflorencie, Scaling of entanglement entropy in the random singlet phase, Phys. Rev. B **72**, 140408(R) (2005).

[49] G. Refael and J. E. Moore, Criticality and entanglement in random quantum systems, J. Phys. A **42**, 504010 (2009).

[50] M. Fagotti, P. Calabrese, and J. E. Moore, Entanglement spectrum of random-singlet quantum critical points, Phys. Rev. B **83**, 045110 (2011).

[51] C. Dasgupta and S.-k. Ma, Low-temperature properties of the random Heisenberg antiferromagnetic chain, Phys. Rev. B **22**, 1305 (1980).

[52] I. Mondragon-Shem, T. L. Hughes, J. Song, and E. Prodan, Topological Criticality in the Chiral-Symmetric AIII Class at Strong Disorder, Phys. Rev. Lett. **113**, 046802 (2014).

[53] R. Vasseur, A. C. Potter, and S. A. Parameswaran, Quantum Criticality of Hot Random Spin Chains, Phys. Rev. Lett. **114**, 217201 (2015).

[54] R. Vasseur, A. J. Friedman, S. A. Parameswaran, and A. C. Potter, Particle-hole symmetry, many-body localization, and topological edge modes, Phys. Rev. B **93**, 134207 (2016).

[55] G. De Tomasi, D. Trapin, M. Heyl, and S. Bera, Anomalous diffusion in particle-hole symmetric many-body localized systems, arXiv:2001.04996.

[56] O. Motrunich, K. Damle, and D. A. Huse, Dynamics and transport in random quantum systems governed by strong-randomness fixed points, Phys. Rev. B **63**, 134424 (2001).

[57] Y. Zhao, F. Andraschko, and J. Sirker, Entanglement entropy of disordered quantum chains following a global quench, Phys. Rev. B **93**, 205146 (2016).

[58] S. Aubry and G. André, Analyticity breaking and Anderson localization in incommensurate lattices, Ann. Israel Phys. Soc. **3**, 18 (1980).

[59] Y. O. Nakagawa, M. Watanabe, H. Fujita, and S. Sugiura, Universality in volume-law entanglement of scrambled pure quantum states, Nat. Commun. **9**, 1635 (2018).

[60] S. Aubry and G. André, Analyticity breaking and Anderson localization in incommensurate lattices, Proceedings, VIII International Colloquium on Group-Theoretical Methods in Physics **3**, 1 (1980).

[61] N. Macé, N. Laflorencie, and F. Alet, Many-body localization in a quasiperiodic Fibonacci chain, SciPost Phys. **6**, 050 (2019).

[62] A. Lazarides, A. Das, and R. Moessner, Periodic Thermodynamics of Isolated Quantum Systems, Phys. Rev. Lett. **112**, 150401 (2014).

[63] R. Fan, Y. Gu, A. Vishwanath, and X. Wen, Emergent Spatial Structure and Entanglement Localization in Floquet Conformal Field Theory, Phys. Rev. X **10**, 031036 (2020).

[64] Y. Li, X. Chen, and M. P. A. Fisher, Quantum Zeno effect and the many-body entanglement transition, Phys. Rev. B **98**, 205136 (2018).

[65] B. Skinner, J. Ruhman, and A. Nahum, Measurement-Induced Phase Transitions in the Dynamics of Entanglement, Phys. Rev. X **9**, 031009 (2019).

[66] C.-M. Jian, Y.-Z. You, R. Vasseur, and A. W. W. Ludwig, Measurement-induced criticality in random quantum circuits, Phys. Rev. B **101**, 104302 (2020).

[67] P. Roushan, C. Neill, J. Tangpanitanon, V. M. Bastidas, A. Megrant, R. Barends, Y. Chen, Z. Chen, B. Chiaro, A. Dunsworth, A. Fowler, B. Foxen, M. Giustina, E. Jeffrey, J. Kelly, E. Lucero, J. Mutus, M. Neeley, C. Quintana, D. Sank *et al.*, Spectral signatures of many-body localization with interacting photons, Science **358**, 1175 (2017).

[68] M. Schreiber, S. S. Hodgman, P. Bordia, H. P. Lüschen, M. H. Fischer, R. Vosk, E. Altman, U. Schneider, and I. Bloch, Observation of many-body localization of interacting fermions in a quasirandom optical lattice, Science **349**, 842 (2015).

[69] T. Brydges, A. Elben, P. Jurcevic, B. Vermersch, C. Maier, B. P. Lanyon, P. Zoller, R. Blatt, and C. F. Roos, Probing Rényi entanglement entropy via randomized measurements, Science **364**, 260 (2019).

[70] E. Mascot, M. Nozaki, and M. Tezuka, Local operator entanglement in spin chains, arXiv:2012.14609.

[71] P. Calabrese and J. Cardy, Time Dependence of Correlation Functions Following a Quantum Quench, Phys. Rev. Lett. **96**, 136801 (2006).

[72] V. Alba and P. Calabrese, Entanglement and thermodynamics after a quantum quench in integrable systems, Proc. Natl. Acad. Sci. (USA) **114**, 7947 (2017).

[73] V. Alba and P. Calabrese, Entanglement dynamics after quantum quenches in generic integrable systems, SciPost Phys. **4**, 017 (2018).

[74] F. J. Dyson, The dynamics of a disordered linear chain, Phys. Rev. **92**, 1331 (1953).